An extended *XMM–Newton* observation of the Seyfert galaxy NGC 4051 – II. Soft X-ray emission from a limb-brightened shell of post-shock gas

K. A. Pounds★ and S. Vaughan

Department of Physics and Astronomy, University of Leicester, Leicester LE1 7RH

ABSTRACT

An extended *XMM–Newton* observation of the Seyfert 1 galaxy NGC 4051 in 2009 revealed a complex absorption spectrum, with a wide range of outflow velocities and ionization states. The main velocity and ionization structure was interpreted in Paper I in terms of a decelerating, recombining flow resulting from the shocking of a still higher velocity wind colliding with the interstellar medium or slower moving ejecta. The high sensitivity of the *XMM–Newton* observation also revealed a number of broad emission lines, all showing evidence of self-absorption near the line cores. The line profiles are found here to be consistent with emission from a limb-brightened shell of post-shock gas building up ahead of the contact discontinuity. While the broad emission lines remain quasi-constant as the continuum flux changes by an order of magnitude, recombination continua of several H- and He-like ions are found to vary in response to the continuum, providing an important key to scaling the ionized flow.

Key words: galaxies: active – galaxies: general – galaxies: individual: NGC 4051 – galaxies: Seyfert – X-rays: galaxies.

1 INTRODUCTION

High-resolution spectra of the bright Seyfert 1 galaxy NGC 4051 obtained by *Chandra* and *XMM–Newton* over the past decade have detected soft X-ray absorption lines indicating a typical outflow velocity of ~500–600 km s^{-1}, with occasional higher blueshifts of up to ~4600 km s^{-1} (Collinge et al. 2001; Ogle et al. 2004; Pounds et al. 2004; Steenbrugge et al. 2009).

A new and much longer *XMM–Newton* observation of NGC 4051 in 2009 has now revealed a high-resolution soft X-ray spectrum with outflow velocities up to ~9000 km s^{-1}. In Pounds & Vaughan (2011, hereafter Paper I), we interpreted an observed correlation of outflow velocity and ionization state in terms of a decelerating and recombining flow, resulting from the shocking of a still higher velocity wind colliding with the interstellar medium (ISM) or slower moving ejecta.

The high sensitivity of the 2009 *XMM–Newton* observation also found several strong and broad emission lines, all showing evidence of self-absorption near the line cores. Broad soft X-ray emission lines have previously been reported for NGC 4051 (Ogle et al. 2004; Steenbrugge et al. 2009), and for several other Seyfert 1 galaxies (Kaastra et al. 2002; Costantini et al. 2007; Smith, Page & Branduardi-Raymont 2007), being interpreted in each case as arising in the inner part of the optical/UV broad-line region (BLR).

In the present paper, we model the broad emission lines in NGC 4051 and consider an alternative origin, in a limb-brightened shell of shocked gas. We note, furthermore, that self-absorption in the shell also offers a natural explanation for a separate low-velocity absorption component, seen across a wide range of ionization states and found in Paper I to break the main velocity–ionization correlation.

A limitation common to many studies of active galactic nucleus (AGN) outflows, which bears directly on estimates of mass, energy and momentum, and hence on AGN feedback, arises from a degeneracy between the radius and particle density of ionized gas in the flow. Attempts to break this degeneracy by detecting flux-linked changes in the ionization state of the absorbing gas have generally been inconclusive. While we find the broad-line emission in NGC 4051 to remain quasi-constant, as the continuum flux changes by an order of magnitude, several radiative recombination continua (RRCs) of H- and He-like ions do vary, apparently in response to the continuum. We examine those data to constrain the recombination time of the photoionized gas and thereby scale the parameters of the flow in NGC 4051.

2 OBSERVATIONS AND DATA ANALYSIS

NGC 4051 was observed by *XMM–Newton* on 15 orbits between 2009 May 3 and June 15, yielding an overall exposure of ~600 ks for each of the reflection grating spectrometers (RGSs), RGS 1 and RGS 2 (den Herder et al. 2001). Full details on the timing, flux

★E-mail: kap@le.ac.uk

levels and X-ray light curves for each satellite orbit of the 2009 observation are included in an accompanying paper on the 'rapid X-ray variability of NGC 4051' (Vaughan et al. 2011).

Fig. 1 illustrates the combined and fluxed RGS spectrum summed over the three lowest flux orbits (4, 11 and 13 in Fig. 2) of the 2009 observation. The emission spectrum is better defined than in any earlier observation of NGC 4051, benefiting from the long exposures and relatively low background prevailing over the relevant part of each orbit.

Among the more prominent features are narrow emission lines identified with forbidden transitions in the He-like ions of Ne IX (rest wavelength 13.698 Å), O VII (22.101 Å) and N VI (29.534 Å). In Paper I, it was suggested that the narrow width and very low velocity of the strong O VII forbidden line might indicate an origin in an accumulation of interstellar gas swept up by multiple forward shocks.

In contrast, it was proposed there that the broad emission components, most obvious in Fig. 1 for O VIII Lyman α (18.968 Å) and the region of the O VII triplet ($\sim$21.6–22.1 Å), but also visible in emission lines of Ne IX, Fe XVII, N VII, N VI and C VI, might arise in a limb-brightened shell of the cooling post-shock flow. We explore that concept further in the present paper.

Also evident in Fig. 1 is absorption at the core of several broad emission lines. It is well known that absorption in a low-velocity flow might be underestimated due to 'filling in' by re-emission from an extended volume of the same ionized gas. Pounds et al. (2004) suggested that this was so for the narrow, low-velocity absorption lines dominating the 2001 *XMM–Newton* observation of NGC 4051. The higher quality data from the 2009 observations now suggest that the interaction of emission and absorption is more complex.

In the remainder of this paper, we explore some general parameters of the broad-line soft X-ray emission in NGC 4051 by examining the velocity profiles of O VIII Lyman α and the O VII triplet (we outline the method of producing the velocity profiles in Appendix A). We then seek to constrain changes in the ionization state, and hence estimate the particle density in the post-shock flow, by a study of the O VIII Lyman α velocity profile and several strong RRCs, as the mean continuum flux level changes.

## 2.1 The velocity profile for O VIII Lyman α

As noted above, the broad emission features are best seen in the low-flux data, due to a higher contrast with the continuum and minimal confusion of low-velocity continuum absorption with the self-absorption in the broad lines. We begin by examining the composite velocity profile of the O VIII Lyman α line for the three lowest flux observations (obs 4, 11 and 13, hereafter the low3 data).

Fig. 3 (top panel) shows the resulting velocity profile, where the broad emission has been visually fitted with a positive Gaussian of width, velocity offset and amplitude corresponding to that used in Paper I to better quantify absorption in the higher flux spectrum. (Although there is some indication that the actual emission profile is more centrally peaked than a single Gaussian, as is also found in broad optical and UV lines, we retain the simpler model as a satisfactory template throughout the present analysis.) Represented in that way, the emission line is blueshifted, with a centroid velocity $v = -750 \, \mathrm{km \, s^{-1}}$ (where $v = 0$ corresponds to the Lyman α source frame wavelength of 18.968 Å) and 1σ width of $1420 \, \mathrm{km \, s^{-1}}$. We note that the measured width greatly exceeds the RGS resolution which corresponds, at $\sim$19 Å, to $\sigma \sim 400 \, \mathrm{km \, s^{-1}}$.

While the single Gaussian is a good fit to the red wing and at the extreme part of the blue wing of the low3 data, strong absorption
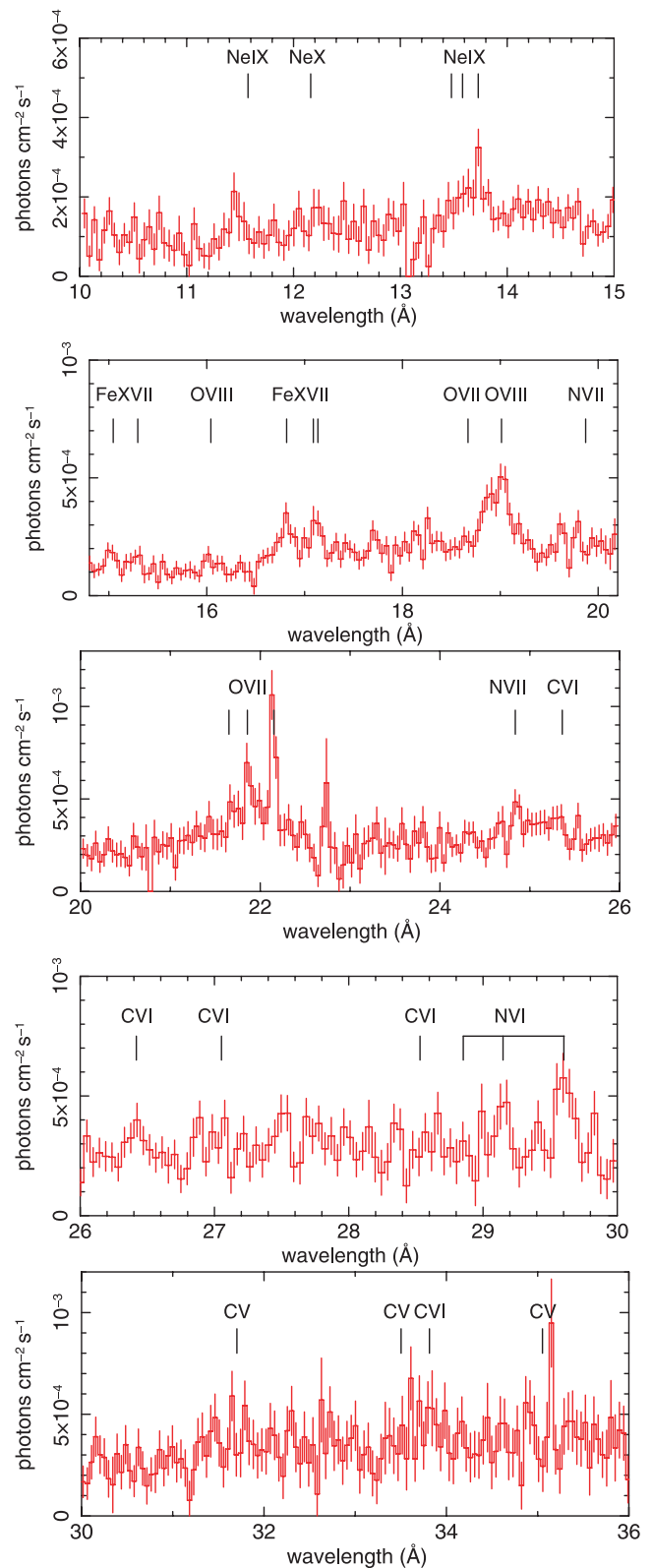
Figure 1. Fluxed RGS spectrum of NGC 4051 summed over three low-flux orbits, showing a dominant emission-line spectrum at lower flux levels. The rest wavelengths of the main candidate emission lines are indicated, adjusted to the observing frame in the plot.
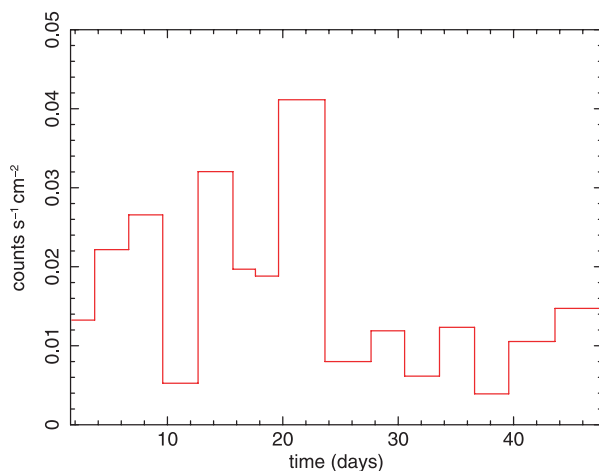
is evident at a similar velocity to the peak of the emission line. It is important to note that the broad-line emission is stronger than the continuum for these low-flux data, with absorption being confined to low velocities. Allowance for the intrinsic RGS resolution confirms that the red wing emission is real, while the absorption appears entirely to the blue side of zero velocity, a strong indication of self-absorption in the emitting gas. With that interpretation, the profile potentially contains important information on the structure and flow geometry of the broad-line gas, a point we take up in Section 4.

The middle panel of Fig. 3 adds the same template emission Gaussian to the composite profile for obs 9–15 (hereafter the low7 data), in the second half of the observation and all of relatively low flux. Again the fit to the red wing of the emission line is good, with the improved statistics sharpening the onset of absorption on the blue side of zero velocity. Continuum absorption is now seen near −5000 and −3500 km s^{-1}, identified as separate high-velocity outflow components in Paper I.

The bottom panel of Fig. 3 shows the composite O VIII Lyman α velocity profile for all the 15 data sets of the 2009 observation. The strong high-velocity outflow reported in Paper I is now seen in the absorption trough extending from ∼−3000 to −7000 km s^{-1}, while a low-velocity continuum absorption component is apparently underlying the broad emission line. More directly relevant to the present study is the excellent visual fit of the low-flux emission template to the all-data broad emission line, again to the red wing and peak, and now also to the blue wing, supporting the working assumption in Paper I that the broad emission lines are quasi-constant throughout the 2009 observation.

In summary, we find the broad emission component of the O VIII Lyman α line to be well described by a positive Gaussian of width 1σ ∼ 1420 km s^{-1} and centred at −750 km s^{-1}, with strong absorption confined to the blue wing of the emission line.

2.2 The velocity profile for the triplet lines of O VII

Broad-line emission is also evident in the region of the O VII triplet (Fig. 1), and appears much broader than for O VIII Lyman α. A similar broad line was reported by Ogle et al. (2004) and Steenbrugge et al. (2009), and interpreted there as arising from an extremely high velocity component of the BLR. We check later whether the improved quality of the new *XMM–Newton* data allows resolution of the broad emission into individual triplet components, as might
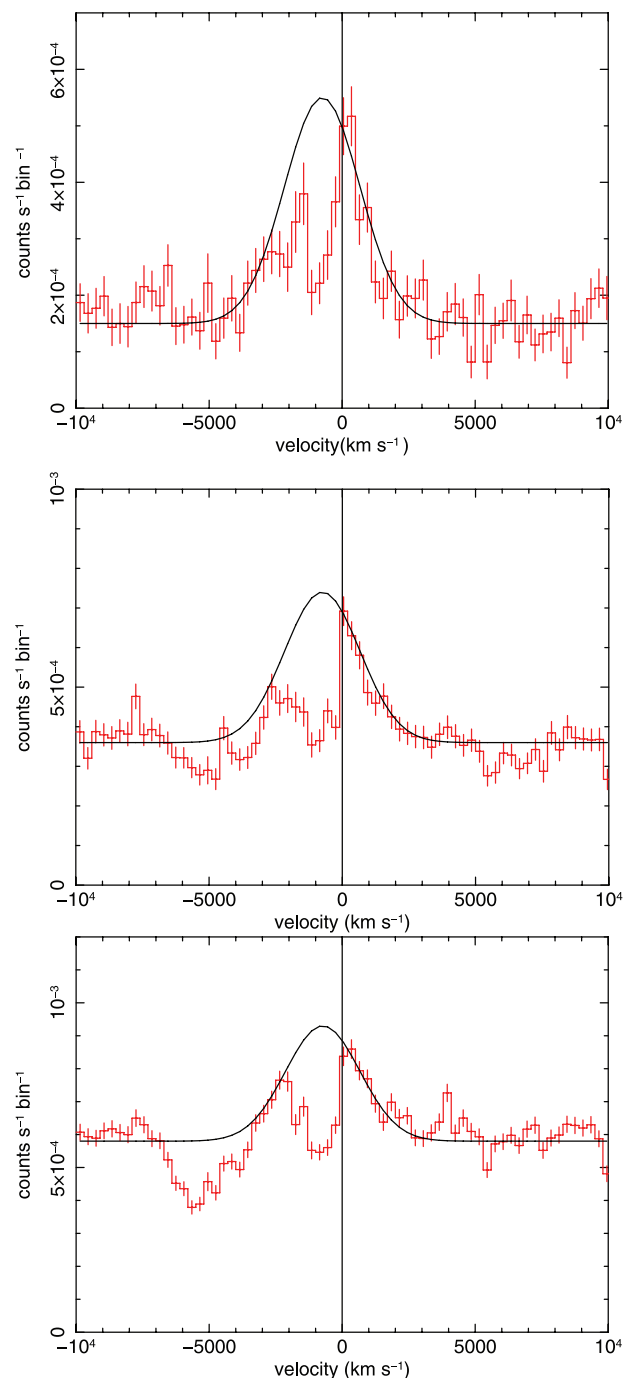
Figure 3. Composite velocity profiles for the O VIII Lyman α line. Top panel: sum of the three lowest flux orbits, showing a broad and blueshifted emission line with strong absorption near the line core. Middle panel: sum of the seven relatively low-flux orbits in the second half of the observation. Bottom panel: velocity profile for the complete 15-orbit observation. The positive Gaussian obtained from fitting the low-flux spectrum in Paper I (and used in quantifying the high-flux absorption) is seen to match the broad emission line in all the three composite velocity profiles, supporting the assumption in Paper I of a quasi-constant emission arising from an extended region of ionized gas.

be expected, adopting individual component profiles as for O VIII Lyman α. However, as a first step, we model the overall emission of the O VII triplet with a single broad component, together with a narrow forbidden line.

Fig. 4 (top panel) shows the O VII low3 velocity profile with the origin set at zero velocity for the intercombination line (rest wavelength 21.807 Å), close to the centre of the triplet. The forbidden line is found to be unresolved, with a 1σ width of 364 ± 37 km s^{-1} (RGS1 1σ width $\sim$350 km s^{-1} at 22 Å), and is blueshifted by 180 ± 37 km s^{-1}. The broad emission component is strongly required, with χ^2 falling from 146/86 degrees of freedom (d.o.f.; for the continuum plus three narrow triplet lines) to 120/87, with a 1σ width of 3400 ± 400 km s^{-1}, a centroid velocity of -70 ± 450 km s^{-1} and an amplitude $1.6 \pm 0.2 \times 10^{-4}$ count s^{-1} bin^{-1}. We note that excess counts in the red wing of the forbidden line suggest that the fit might be affected by ignoring residual absorption in the O VI line (rest wavelength 22.019 Å), found to be strong in Paper I.

The middle panel of Fig. 4 shows a further fit, with the addition of narrow resonance and intercombination line emission, and a negative Gaussian to allow for the O VI absorption. The outcome is a further improved fit (χ^2/d.o.f. = 96/81), with the broad line width increasing to 4400 ± 730 km s^{-1}. The amplitude of the broad line is only marginally reduced by the inclusion of the narrow emission components, both of which appear to be affected by absorption, the intercombination line probably by the O VI satellite line (21.79 Å) and the resonance line by self-absorption. The result is that both lines appear redshifted, in marked contrast to the forbidden line. The resonance line is most strongly affected, with the observed emission centroid at an unlikely redshift of 470 ± 140 km s^{-1}. We return to this in Section 2.3.

On the basis of the above profile fitting, we find that the O VII broad emission line is remarkably strong, the flux within the single broad-line fit being more than twice that in the forbidden line. However, the likelihood remains that the broad emission is a blend from all three components of the triplet, assuming that the origin is indeed velocity broadening. It would then be particularly interesting to resolve the separate components as their respective strengths could be an important diagnostic of the density and mode of excitation of the emitting gas.

To seek such a resolved profile, we repeated the fit to the low-flux data, replacing the single broad component with three separate components, each with a blueshift and a width of -750 and 1420 km s^{-1}, respectively, the template from the fit to O VIII Lyman α. The amplitude of each line was left free. A further negative Gaussian was added to allow for absorption in the O VII resonance line.

The main result of this further fit (Fig. 4, lower panel) was to quantify broad components of the separate triplet lines, finding respective amplitudes of $2.2 \pm 0.5 \times 10^{-4}$ for the forbidden line, and $1.0 \pm 0.3 \times 10^{-4}$ count s^{-1} bin^{-1} for the resonance and intercombination lines. The narrow forbidden line velocity was unchanged and again unresolved, with a 1σ width of 310 ± 50 km s^{-1}. The absorption lines of O VI and O VII yielded low outflow velocities consistent with the values obtained in Paper I.

Although this more complex fit was statistically no better than the middle panel fit, it did confirm the broad emission in O VII to be physically compatible with that seen in O VIII Lyman α; moreover, finding the strongest broad component from the forbidden line would rule out a high density for the emitting gas (and perhaps argue against the BLR origin proposed elsewhere).

2.3 Implications of a strongly self-absorbed resonance line

The diagnostic power of the He-like triplets in NGC 4051 and other type 1 AGN has often been severely limited by strong absorption of the resonance line, a situation we again find in the 2009
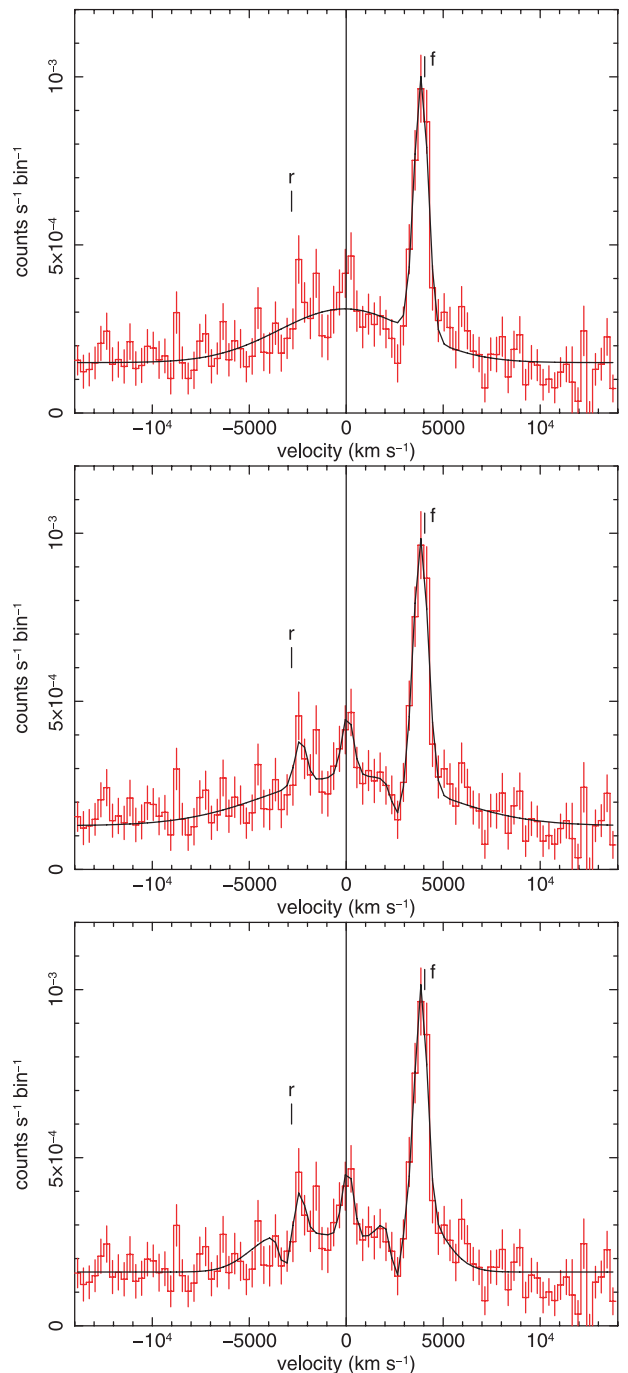
Figure 4. Composite velocity profile for the three lowest flux orbits in the region of the O VII triplet, expressed in terms of a velocity shift from the rest wavelength of the intercombination line. The top panel shows a fit with a single broad emission line in addition to the narrow forbidden line. The middle panel is a statistically improved fit with the addition of narrow intercombination and resonance emission lines and allowing for residual O VI absorption near the blue wing of the forbidden line. The bottom panel shows a further fit with separate broad emission components for the three triplet lines.

XMM–Newton data. In particular, a dominant forbidden line cannot be taken as definitive evidence of a pure photoionized gas (Porquet & Dubau 2000). The observation of a weak and redshifted line in O VII suggests that the resonance line emission may be substantially
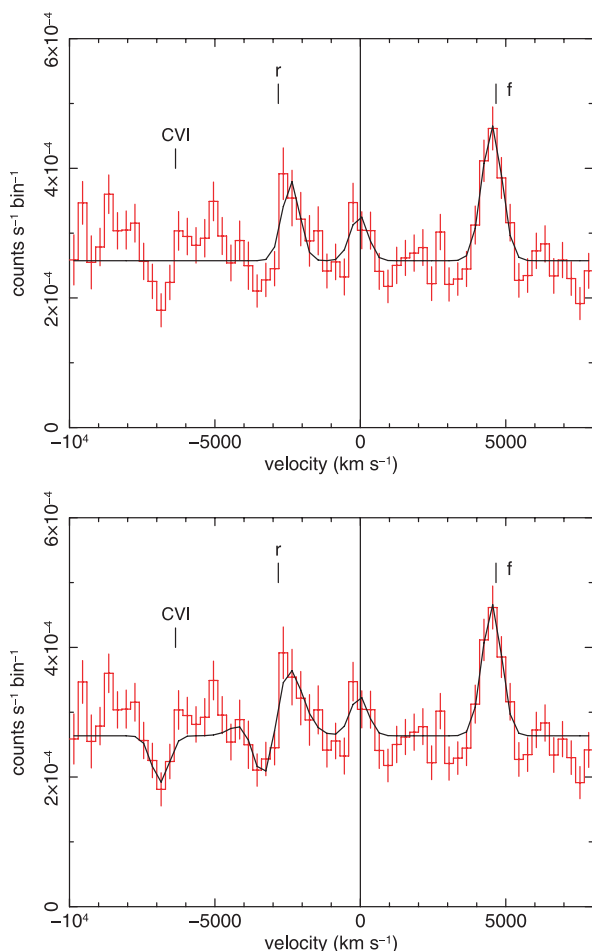
Figure 5. Velocity profiles for the N VI triplet from a composite of the low7 data, centred at zero velocity for the intercombination line. Zero-velocity positions of the forbidden and resonance lines are indicated, as is that of C VI Lyman β. The bottom panel includes a P Cygni fit to the N VI resonance line.

underestimated in NGC 4051, raising the possibility that the soft X-ray emission has a significant thermal component, which would be consistent with strong two-body cooling in the later stages of the post-shock flow. We also note that higher temperature (broader) RRCs would not be easy to resolve from the continuum, even in spectra of the present quality.

While it is difficult to constrain the core O VII resonance emission in NGC 4051, the N VI triplet appears less strongly self-absorbed in the low-flux data (Fig. 5, top panel). The velocity profile for N VI, again centred on the intercombination line (29.082 Å), shows an unresolved forbidden line (1σ width of $330 \pm 50\,\mathrm{km\,s^{-1}}$) with a blueshifted velocity of $v = -140 \pm 50\,\mathrm{km\,s^{-1}}$. The narrow intercombination line is weaker, but the red wing of the resonance line is much better defined than for O VII.

In order to estimate the true strength of the resonance emission line, we repeated the N VI profile fit, including resonance and absorption lines initially fixed at velocities (relative to the source frame) of -180 and $-400\,\mathrm{km\,s^{-1}}$, respectively, taken from the measured positions of the N VI forbidden and C VII Lyman β lines in the same plot. The outcome was a fit to the resulting P Cygni profile of the N VI resonance line (Fig. 5, bottom panel), with emission and absorption components of similar strength. In particular, the reso-

nance emission amplitude, $2.4 \pm 0.7 \times 10^{-4}\,\mathrm{count\,s^{-1}\,bin^{-1}}$, was now comparable to the forbidden line, and inconsistent with a pure photoionized gas. While photoexcitation will increase the relative strength of the resonance line (and has been shown to provide a good fit to the soft X-ray spectra of NGC 1068; Kinkhabwala et al. 2002), a strong resonance line could indicate a significant thermal emission component in NGC 4051.

3 EVIDENCE FOR FLUX-LINKED VARIABILITY IN THE IONIZATION STATE OF THE SHOCKED OUTFLOW

The continuum absorption was found in Paper I to have a well-determined velocity and ionization structure. In terms of a cooling post-shock flow, the observed correlation of velocity and ionization parameter requires the recombination time to be sufficiently short for the gas to adjust along the flow. To check for that consistency requires the flow dimensions to be known, which in turn depends on breaking the degeneracy between radial distance (from the ionizing source) and the particle density at some point along the flow.

Establishing a flux-linked variability in the ionization structure of the flow, and hence constraining the related recombination rate and gas density, is also of key importance in estimating the mass, energy and momentum of the outflow. To pursue those aims, we have examined the velocity profiles for each individual orbit of the 2009 observation. We focus here on profiles from observations of relatively low mean flux (and thereby less affected by absorption), and immediately following the highest flux observation (obs 8 in Fig. 2). We again show the profile centred on O VIII Lyman α, which also covers the region of the N VII RRC.

Fig. 6 reproduces the profiles for obs 9, 10 and 11. In each case, the low-flux Gaussian template represents a satisfactory visual fit to the red (unabsorbed) wing of the broad emission line. To the blue side, only obs 11 (bottom panel) is a good fit, with absorption more strongly affecting the higher flux profiles. Nevertheless, to first order, the broad-line emission appears essentially unchanged over the three successive orbits.

However, the obs 9 profile shows a strong excess to the blue side of $v = -6000\,\mathrm{km\,s^{-1}}$ (corresponding to the threshold wavelength of the N VII RRC). In obs 10, some 2 d later, the RRC is noticeably weaker, while in a further 4 d, by obs 11, it has faded from view.

Although the RRC profile is not well determined, and might be affected by O VII absorption, an apparent blueshift of $\sim 2000\,\mathrm{km\,s^{-1}}$ in the peak flux is of particular interest, in suggesting an origin in the intermediate-velocity outflow seen in absorption (Paper I). Importantly, if confirmed, that identification would link the intermediate-velocity gas with a region in the flow where fully stripped nitrogen is recombining over several days as the X-ray flux falls back from its peak in obs 8. A recombination time-scale of ~ 2–6 d for the relevant component in the outflow would then correspond to a particle density $\sim 5 \times 10^5\,\mathrm{cm^{-3}}$.

3.1 Other RRCs

The potential importance of a variable N VII RRC, apparently responding to an earlier peak continuum flux, increases the interest in examining other RRCs covered by the RGS data. The O VII RRC (threshold wavelength 16.769 Å) is found to be strong, and apparently variable, but its measurement is impeded by strong nearby Fe XVII lines and a location at the long-wavelength edge of the Fe
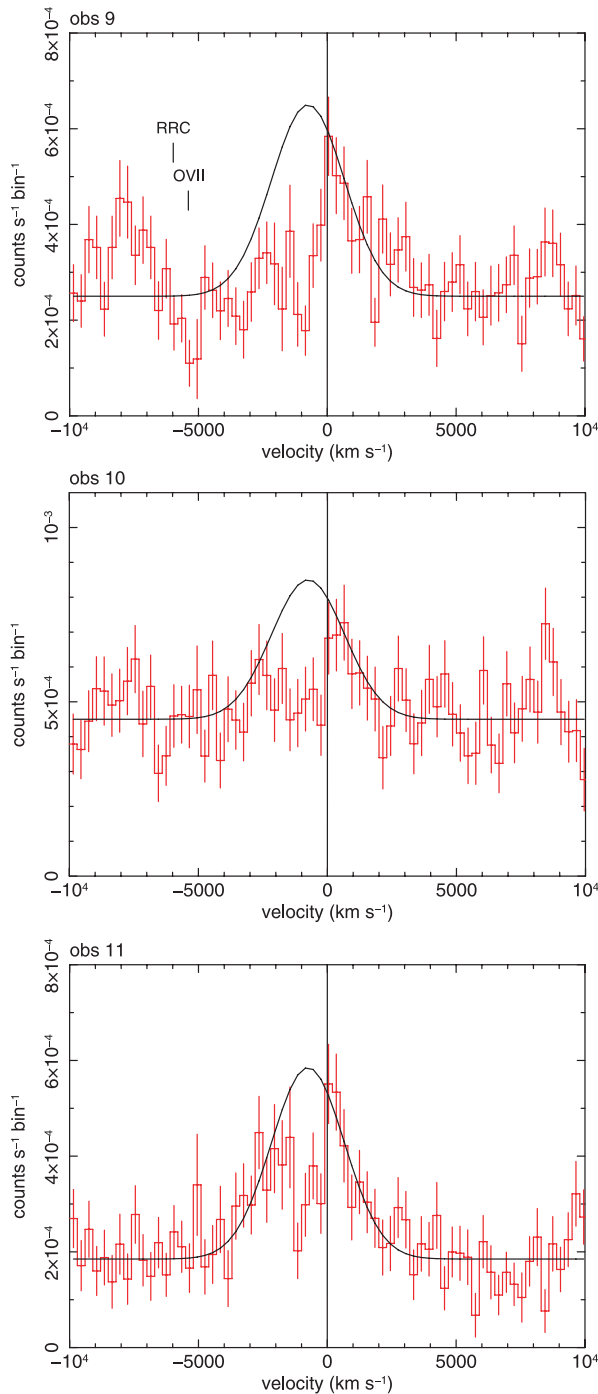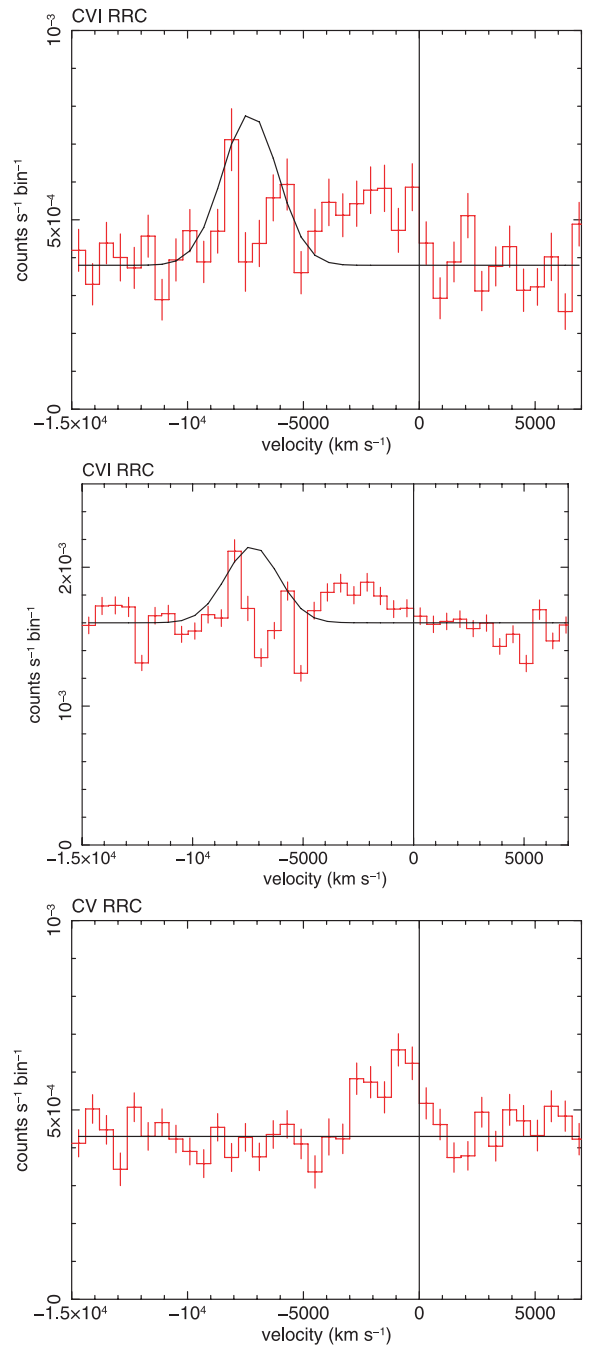
Figure 6. Velocity profiles centred on the O VIII Lyman α line for three successive orbits following several days of high continuum flux. A strong and possibly blueshifted N VII RRC is seen to fade over several days.

Figure 7. Top and middle panels: velocity profiles of the C VI RRC for two different continuum levels. Also shown is the template Gaussian fit to the N VII Lyman α line clarifying the resolution of the RRC. The peak RRC flux is seen to shift to the blue for higher continuum levels, as also found for the N VII RRC. Bottom panel: the C V RRC is always seen at the zero-velocity threshold.

UTA. The O VIII and Ne IX RRCs fall in regions where the RGS sensitivity is falling. However, both C V and C VI are found to exhibit strong RRCs, and are less affected by other spectral features.

The top two panels of Fig. 7 show velocity profiles for the C VI RRC, centred at the threshold wavelength of 25.303 Å (note that the binning here is 600 km s^{-1}, with an extended range to the blue side to cover the region of the N VII Lyman α line at 24.781 Å and to better determine the continuum level). An emission-line template is added visually to the top panel and carried over to the higher flux

level profile in the middle panel, the primary aim here being to show that the C VI RRC is well resolved.

As with the N VII RRC, the peak C VI RRC flux is seen to shift to the blue as the continuum level increases, and in this case there are no likely absorption lines to affect the RRC profile close to the threshold wavelength. The similarity in the C VI and N VII RRC blueshifts at higher continuum levels strengthens a direct association

of the recombining plasma with the strong absorption observed in the same higher level ions (Paper I).

Furthermore, tracking the C VI RRC through individual orbits shows a similar pattern to the N VII RRC, again indicating a response time for the intermediate-velocity gas of a few days. In contrast, the lower level C V RRC (31.63 Å) shown in Fig. 7 (bottom panel) only appears at the zero-velocity threshold, consistent with the low absorption velocities characteristic for that ion.

In summary, we find the RRCs of N VII and C VI to vary in strength and velocity profile over several days and in a manner apparently dependent on the continuum flux level. We interpret the variability as from enhanced photoionization of the high-velocity flow when the continuum flux level is high, being followed by strong recombination over the following days of reduced flux level. The velocity and ionization gradients found in the absorption spectra (Paper I) then explain the differences between the RRCs of N VII, C VI and the lower ionization state of C V.

The best determined RRC profiles all indicate a relatively low temperature of $\sim 7 \pm 2$ eV.

4 DISCUSSION

In Paper I, we reported a rich absorption-line spectrum from the 2009 *XMM–Newton* observation of NGC 4051, revealing the presence of an ionized outflow with a wide range of velocities and ionization parameter. The absorption-line velocity structure and a broad correlation of velocity with ionization parameter were shown there to be consistent with an outflow scenario where a highly ionized, high-velocity wind runs into the ISM or previous ejecta, losing much of its kinetic energy in the resultant strong shock (King 2010). With the strong immediate post-shock cooling likely to be dominated by Compton scattering of the AGN thermal continuum (King 2003), we also noted that a quasi-constant soft X-ray emission component might be evidence of further energy loss as the post-shock gas slowed and recombined ahead of the contact discontinuity.

A second outstanding feature of the soft X-ray data from the 2009 observation was a complex emission-line spectrum, particularly evident at low continuum flux levels, with velocity-broadened emission from several H- and He-like resonance lines, as well as a number of strong RRCs. Broad emission lines of O VII and O VIII have been reported previously from NGC 4051 (Ogle et al. 2004; Steenbrugge et al. 2009), and attributed to scattering of the AGN X-ray continuum from high-velocity clouds in the BLR. An alternative interpretation, outlined here, envisages the broad emission lines arising from the limb-brightened shell of shocked gas building up ahead of the contact discontinuity. On this alternative picture, the line broadening primarily arises from the angular divergence of the flow at the bright limb of the expanding spherical shell.

An optically thin spherical shell would produce an emission line centred on zero velocity (in the AGN rest frame). Since in a spherical geometry the absorbing gas will always have a positive line-of-sight velocity relative to the emission, self-absorption in the shell will set the onset of absorption at zero velocity. The latter is precisely what the data (e.g. Fig. 3) show, although the peak of emission is shifted to the blue.

Fig. 8 sketches the geometry of such a limb-brightened shell, where the broad emission line of O VIII Lyman α is depicted arising from a near-orthogonal component of the high-velocity radial flow, seen in the absorption in the line of sight to the continuum, but now with lower apparent velocities observed in emission from the limb. In the figure, for a typical post-shock absorption velocity of 5000 km s^{-1} (Paper I), the red and blue wings [at half-width at
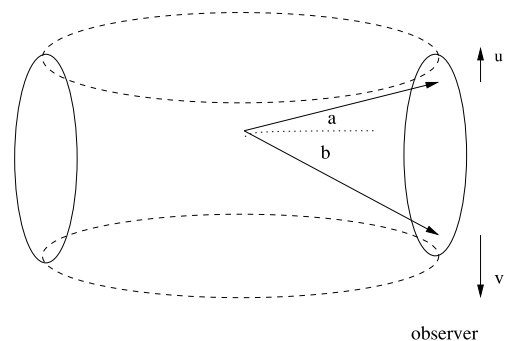
Figure 8. Geometry of a limb-brightened shell, where the broad line of O VIII Lyman α is explained as emission from the high-velocity radial flow, seen in continuum absorption when in line of sight to the nucleus. The indicated flow lines correspond to the red (u) and blue (v) wings of the emission-line profile when viewed by the observer. The central offset corresponds to a dominantly near-sided/approaching outflow.

half-maximum (HWHM)] of the O VIII Lyman α line correspond to rearward and forward inclinations $a \sim 12°$ and $b \sim 30°$, respectively.

While the blue offset in the observed broad emission-line profiles might be an artefact of self-absorption, it is perhaps more likely evidence of a dominantly near-sided/approaching outflow. However, we also note that the red wing in the O VIII Lyman α line is broader than the instrument response, indicating that at least part of the far, receding side of the shell is visible.

The putative torus is an obvious candidate for obscuring part of the receding flow in the shell, given the estimated shell radius of $\sim 7 \times 10^{17}$ cm (Paper I). In that context, it is interesting to note that a strong blueshifted asymmetry in the [O III] line profile of NGC 4051 was described by Veilleux (1991) to 'favour radial motion and a source of obscuration'. On still larger scales, a narrower, forward-projected conical outflow was observed in the [O III] imaging and the spectroscopy of NGC 4051 (Christopoulou et al. 1997).

With the flow of gas in the limb-brightened shell near-orthogonal to the line of sight, the geometry of Fig. 8 also offers a natural explanation of the separate low-velocity absorption component, found in Paper I to occur over a wide range of ionization, in contrast to the higher velocity absorption where the velocity and ionization parameter are strongly correlated.

In contrast to the quasi-constant broad emission lines, the RRCs of N VII and C VI are found to vary, in both strength and profile, on a time-scale of days. Given that the change appears to respond to the continuum flux level, we interpret the variability in terms of the recombination time and hence derive a particle density for the relevant intermediate-velocity/ionization region in the post-shock flow of the order of 5×10^5 cm^{-3}.

The relatively short recombination time provides an important consistency check on the observed velocity/ionization gradient in the absorption spectra reported in Paper I, and shown there to be a simple consequence of mass conservation. In particular, that outcome requires the flow to recombine sufficiently quickly as it decelerates, in order to maintain the observed velocity/ionization correlation. With an estimated shell thickness (Paper I) of $\sim 4 \times 10^{15}$ cm, and for a mean velocity of ~ 4000 km s^{-1}, the shell transit time of a few months is comfortably longer than the recombination time along the flow. We also note that the relatively low density in the post-shock gas is consistent with finding a broad component to the O VII forbidden line.

Finally, while the strong RRCs are indicative of a dominantly photoionized gas, as is the low temperature $kT \sim 7$ eV, we also find

a narrow resonance emission line in the N VI triplet comparable in strength to the narrow forbidden line, which could imply an electron temperature an order of magnitude higher (fig. 7 in Porquet & Dubau 2000) and a significant thermal emission component.

However, some of the clearest soft X-ray emission spectra to date, from observations of the bright Seyfert 2 galaxies, Mrk 3 (Sako et al. 2000) and NGC 1068 (Kinkhabwala et al. 2002; Ogle et al. 2003), have shown that the X-ray emission in those objects is explained by radiative recombination and decay in an outflow which is photoionized and photoexcited by the central continuum, with no significant thermal emission.

Nevertheless, the obscuring torus in such a type 2 object is likely to hide emission from the innermost, high-velocity flow. In that respect, it is interesting to recall that *XMM–Newton* EPIC spectra of a sample of Two Micron All Sky Survey (2MASS) sources suggested that the 'hidden' soft X-ray emission could be relatively strong (Pounds & Wilkes 2007; Wilkes, Pounds & Schmidt 2008), while we also note that the high-quality soft X-ray spectra of type 2 Seyferts show no evidence for broad-line emission.

In that wider context, the 2009 *XMM–Newton* observation of NGC 4051 may offer one of the best opportunities to date to study the full soft X-ray emission spectrum of a Seyfert galaxy. On our interpretation, at least, the inner regions are of special interest in harbouring shocks that are likely to strongly affect the dynamics of the subsequent outflow and its interaction with the host galaxy.

5 SUMMARY

Broad emission lines of O VIII Lyman α and the O VII triplet, possibly including a broad component of the forbidden line, are found to be strong throughout the 2009 *XMM–Newton* observation of NGC 4051.

The low centroid velocity of the O VIII Lyman α broad line is consistent with an origin in the limb-brightened shell of post-shock gas, with emission from the near-orthogonal component of the flow seen in the continuum absorption at $\sim -5000\,\mathrm{km\,s^{-1}}$.

The same geometry provides a natural explanation for the sharp onset of absorption to the blue side of zero velocity, found in all individual velocity profiles, being interpreted as a consequence of the radial flow through the limb-brightened shell, leading all absorbing gas to have a blueshift relative to the source of emission.

The detection of RRCs of N VII and C VI, which vary in both flux and velocity profile as the continuum level changes, has yielded an important measure of the recombination time-scale for ionized gas in the related high-velocity flow. Breaking the degeneracy between radius and particle density, which so often limits the assessment of AGN outflows, has allowed the radius and thickness of the shell of post-shock gas to be estimated, and in turn has confirmed that the high-velocity flow is able to recombine sufficiently fast to maintain the observed correlation of ionization parameter and velocity reported in Paper I.

Strong low-velocity absorption renders the O VII resonance line essentially unconstrained, and leads to narrow components of O VIII Lyman α and other resonance lines in NGC 4051 (and perhaps more generally in type 1 Seyferts) to be poorly determined. Together with the observational difficulty of detecting much broader (and hotter) RRCs, we conclude that a significant thermal contribution to the soft X-ray emission of NGC 4051 cannot be ruled out. Nevertheless, with the relatively low particle densities in the post-shock flow, two-body cooling is likely to remain less important than Compton cooling which we have argued (Paper I; King 2003) will be strong so close to the AGN continuum source.

REFERENCES

Christopoulou P. E., Holloway A. J., Steffen W., Mundell C. G., Thean A. H. C., Goudis C. D., Meaburn J., Pedlar A., 1997, MNRAS, 284, 385
Collinge M. J. et al., 2001, ApJ, 557, 2
Costantini et al., 2007, A&A, 461, 121
den Herder J. W. et al., 2001, A&A, 365, L7
Kaastra J. S. et al., 2002, A&A, 386, 427
King A. R., 2003, ApJ, 596, L27
King A. R., 2010, MNRAS, 402, 1516
Kinkhabwala A. et al., 2002, ApJ, 575, 732
Ogle P. M., Brookings T., Canizares C. R., Lee J. C., Marshall H. L., 2003, A&A, 402, 849
Ogle P. M., Mason K. O., Page M. J., Salvi N. J., Cordova F. A., McHardy I. M., Priedhorsky W. C., 2004, ApJ, 606, 151
Porquet D., Dubau J., 2000, A&A, 143, 495
Pounds K. A., Vaughan S., 2011, MNRAS, 413, 1251
Pounds K. A., Wilkes B. J., 2007, MNRAS, 380, 1341
Pounds K. A., Reeves J. N., Page K. L., O'Brien P. T., 2004, ApJ, 616, 696
Sako M., Kahn S. M., Paerels F., Liedahl D. A., 2000, ApJ, 543, L11
Smith R. A. N., Page M. J., Branduardi-Raymont G., 2007, A&A, 461, 135
Steenbrugge K. C., Fenovcik M., Kaastra J. S., Costantini E., Verbunt F., 2009, A&A, 496, 107
Vaughan S., Uttley P., Pounds K. A., Nandra K., Strohmeyer T. E., 2011, MNRAS, 413, 2489
Veilleux S., 1991, ApJ, 369, 331
Wilkes B. J., Pounds K. A., Schmidt G. D., 2008, ApJ, 680, 110

APPENDIX A: VELOCITY PROFILES FROM RGS SPECTRA

In this section, we describe the method used to produce the line velocity profiles which are the basis of the analysis in this paper. We choose the velocity plots as they provide a convenient (and accurate) way of combining different data sets, and present the parameters of interest in the directly relevant velocity coordinates. Each RGS observation was first processed using RGSPROC to produce a set of first-order source and background spectra, along with appropriate response matrices, from each of RGS1 and RGS2, with 3400 wavelength channels.

The simplest way to produce a velocity profile for several lines from several observations is to sum the counts in each spectral channel across the observations, transform the wavelengths of the channels around each line of interest to velocity shifts relative to the (source-frame) wavelength of the line and then average (or sum) over the different lines. Unfortunately, this simple procedure is complicated by three facts about the RGS data. First, the RGS effective area can change sharply due to bad pixels, columns or even whole CCDs. Secondly, small differences in the pointings between the observations mean that the wavelength-channel conversion differs slightly between observations. (At least, this is true for the standard products produced by RGSPROC.) And thirdly, the wavelength resolution of the RGS is approximately constant across the spectral range, meaning that the velocity resolution differs for lines at

different wavelengths. Taken together, the first two facts mean that co-adding spectra by summing the counts in each channel will result in a degradation (blurring) of the line response function, and may produce spurious line-like features (due to narrow 'dropouts' in the spectra) if not corrected using an effective area curve computed for the merged data. The third point means that the velocity bins for one line will not be well matched to those of other lines, making it difficult to average the counts in velocity bins over different lines.

The solution we employ is to convert each spectrum from counts per channel, with a corresponding channel to wavelength range conversion, to a list of wavelengths for each event. We do this by randomizing the wavelength of each event in a given spectral channel, in a given observation, within the wavelength range of the channel specified in the appropriate (observation-specific) response matrix. This effectively 'unbins' the spectrum, but as the wavelength range of each channel (in the 3400-channel RGS spectral products) is far smaller than the resolving power of the RGS, the randomization within a given channel leads to negligible degradation of the spectral resolution. The wavelengths of the counts around specific lines of interest can be converted to velocity shifts (after corrected for the source's systemic redshift), and the counts rebinned into velocity bins of width Δv. The counts per velocity bin are then summed over different observations and different lines to produce a composite line profile in velocity space. Error bars are computed assuming simple counting statistics (i.e. Poissonian fluctuations within each velocity bin). The same procedure is applied to the background spectra to produce a composite background spectrum in velocity space.

The complex changes in effective area as a function of wavelength mean that the relative weighting of source and background spectra is itself a complex function of wavelength. The effective exposure time per velocity bin of the composite was calculated by summing the product of the individual exposure times of the observations and a wavelength-dependent quality function to account for 'dropouts' in individual spectra (caused by bad CCD columns or missing chips, which contributed zero effective exposure for certain wavelengths). This was converted to velocity space (around the lines of interest), averaged in velocity bins and summed over the different lines. The result is the average exposure time each velocity bin acquired from each observation and each line contributing to the spectrum. This was then used to calculate the effective count rate (count s^{-1}) per velocity bin for both source and background spectra.

The wavelength-dependent scaling of source and background extraction regions was calculated by summing the effective area curves (as a function of wavelength) of each observation, weighted by the observational exposure time, separately for the source and background data. The ratio of the resulting curves gives the source/background scaling as a function of wavelength. This scaling function was then converted to velocity shifts (around the lines of interest), averaged in velocity bins and summed over the different lines, and the result was used to perform the velocity-dependent background subtraction. The final result is a background-corrected count rate as a function of velocity.

This paper has been typeset from a TEX/LATEX file prepared by the author.